
FERMION CONDENSATION: A STRANGE IDEA SUCCESSFULLY EXPLAINING BEHAVIOR OF NUMEROUS OBJECTS IN NATURE

V.R. SHAGINYAN,¹ M.YA. AMUSIA,² K.G. POPOV³

¹Petersburg Nuclear Physics Institute, RAS
(Gatchina, 188300, Russia; e-mail: vrshag@thd.pnpi.spb.ru)

²Racah Institute of Physics, Hebrew University
(Jerusalem 91904, Israel)

³Komi Science Center, Ural Division, RAS
(Syktyvkar, 167982, Russia)

PACS 71.27.+a, 71.10.Hf,
73.43.Qt
©2010

Strongly correlated Fermi systems are among the most intriguing, best experimentally studied, and fundamental systems in physics. These are, however, in defiance of theoretical understanding. The ideas based on the concepts like Kondo lattice and involving quantum and thermal fluctuations at a quantum critical point have been used to explain the unusual physics. Alas, being suggested to describe one property, these approaches fail to explain the others. This means a real crisis in theory suggesting that there is a hidden fundamental law of nature, which remains to be recognized. A theory of fermion condensation quantum phase transition, preserving the extended quasiparticles paradigm and intimately related to the unlimited growth of the effective mass as a function of the temperature, magnetic field, etc., is capable to resolve the problem. We discuss the construction of the theory and show that it delivers theoretical explanations of the vast majority of experimental results in strongly correlated systems such as heavy-fermion metals and quasi-two-dimensional Fermi systems. Our analysis is placed in the context of recent salient experimental results. Our calculations of the non-Fermi liquid behavior, the scales, and thermodynamic and transport properties are in good agreement with the heat capacity, magnetization, longitudinal magnetoresistance, and magnetic entropy obtained in remarkable measurements on the heavy-fermion metal YbRh₂Si₂. Using two-dimensional ³He as an example, we demonstrate that the main universal features of its experimental temperature T - density x phase diagram resemble those of the heavy-fermion metals. We propose a simple expression for the effective mass, describing all diverse experimental facts on the ³He in the unified manner and demonstrating that the universal behavior of the effective mass coincides with that observed in heavy-fermion metals.

1. Introduction

Strongly correlated Fermi systems represented by heavy-fermion (HF) metals, high-temperature superconductors, and quasi-two-dimensional ³He are among the most intriguing, best experimentally studied, and fundamen-

tal systems in physics [1]. This is also a field never far from applications in the synthesis of novel materials for cryogenics, rare earth magnets, and applied superconductivity. Their behavior is so unusual that the traditional Landau quasiparticles paradigm is not applied to it. The paradigm states that the properties is determined by quasiparticles, whose dispersion is characterized by the effective mass M^* which is independent of the temperature T , number density x , magnetic field B , and other external parameters. The above systems are, however, in defiance of the theoretical understanding. The ideas based on the concepts (like Kondo lattice; see, e.g., [2]) involving quantum and thermal fluctuations at a quantum critical point (QCP) have been used to explain the unusual physics of these systems known as non-Fermi liquid (NFL) behavior [1–4]. Alas, being suggested to describe one property, these approaches fail to explain the others. This means a real crisis in theory suggesting that there is a hidden fundamental law of nature, which remains to be recognized [5]. It is widely believed that utterly new concepts are required to describe the underlying physics. There is a fundamental question: how many concepts do we need to describe the above physical mechanisms? This cannot be answered on purely experimental or theoretical grounds. Rather, we have to use both of them.

Usual arguments that quasiparticles in strongly correlated Fermi liquids “get heavy and die” at a quantum critical point commonly employ the well-known formula based on assumptions that the z -factor (the quasiparticle weight in the single-particle state) vanishes at the points of second-order phase transitions [6]. However, it has been shown that this scenario is problematic [7]. A concept of fermion condensation quantum phase transition (FCQPT) preserving quasiparticles and intimately re-

lated to the unlimited growth of M^* had been suggested [8–11]. Studies show that it is capable to deliver an adequate theoretical explanation of the vast majority of experimental results for different HF metals [12–14]. In contrast to the Landau paradigm based on the assumption that M^* is a constant, M^* in FCQPT approach strongly depends on T , x , B , etc. Therefore, in accord with numerous experimental facts, the extended quasiparticles paradigm is to be introduced. The main point here is that the well-defined quasiparticles determine as before the thermodynamic and transport properties of strongly correlated Fermi-systems, while M^* becomes a function of T , x , and B , and the dependence of the effective mass on T , x , and B gives rise to the non-Fermi liquid (NFL) behavior [10, 12–17].

In this review, we discuss the construction of a theory based on the above FCQPT approach and its application to the analysis of a wide variety of experimentally observed phenomena in microscopically different strongly correlated Fermi systems like heavy-fermion metals and quasi-two-dimensional ^3He . We analyze the NFL behavior of strongly correlated Fermi systems and show that this is generated by the dependence of the effective mass on the temperature, number density, and magnetic field at FCQPT. We demonstrate that the NFL behavior observed in the transport and thermodynamic properties of HF metals can be described in terms of the scaling behavior of the normalized effective mass. This allows us to construct the scaled thermodynamic and transport properties extracted from experimental facts in a wide range of the variation of a scaled variable. We show that “peculiar points” of the normalized effective mass give rise to the energy scales observed in the thermodynamic and transport properties of HF metals. Our calculations of the thermodynamic and transport properties are in good agreement with the heat capacity, magnetization, longitudinal magnetoresistance, and magnetic entropy obtained in remarkable measurements on the heavy-fermion metal YbRh_2Si_2 [18–21].

2. Fermion Condensation Quantum Phase Transition

We start with visualizing the main properties of FCQPT. To this end, consider the density functional theory for superconductors (SCDFT) [22]. SCDFT states that, at a fixed temperature T , the thermodynamic potential Φ is a universal functional of the number density $n(\mathbf{r})$ and the anomalous density (or the order parameter) $\kappa(\mathbf{r}, \mathbf{r}_1)$ and provides a variational principle to determine the densities [22]. At the superconducting transition tempera-

ture T_c , a superconducting state undergoes the second-order phase transition. Our goal now is to construct a quantum phase transition which evolves from the superconducting one. In that case, the superconducting state takes place at $T = 0$, while there is a normal state at finite temperatures. This means that the anomalous density in this state is finite, while the superconducting gap vanishes. For the sake of simplicity, we consider a homogeneous Fermi (electron) system.

Let us assume that the coupling constant λ of the pairing interaction vanishes, $\lambda \rightarrow 0$, making vanish the superconducting gap at any finite temperature. Then the thermodynamic potential reduces to the ground state energy E which turns out to be a functional of the occupation number $n(\mathbf{p})$ since $\kappa = \sqrt{n(1-n)}$ [16, 17, 22, 24, 25]. Upon minimizing E with respect to $n(\mathbf{p})$, we obtain

$$\frac{\delta E}{\delta n(\mathbf{p})} = \varepsilon(\mathbf{p}) = \mu, \quad (1)$$

where μ is the chemical potential. It is seen from Eq. (1) that, instead of the Fermi step, we have $0 < n(p) < 1$ in a certain range of momenta $p_i \leq p \leq p_f$ with κ to be finite in this range. Thus, the step-like Fermi filling inevitably undergoes restructuring and forms the fermion condensate (FC), as soon as Eq. (1) possesses not-trivial solutions at some point $x = x_c$, when $p_i = p_f = p_F$ [8, 12, 13]. Here, p_F is the Fermi momentum, and $x = p_F^3/3\pi^2$.

At any small but finite temperature, the anomalous density κ (or the order parameter) decays, and this state undergoes the first-order phase transition and converts into a normal state characterized by the thermodynamic potential Φ_0 . At $T \rightarrow 0$, the entropy $S = -\partial\Phi_0/\partial T$ of the normal state is given by the well-known relation [26]

$$S_0 = -2 \int [n(\mathbf{p}) \ln(n(\mathbf{p})) + (1-n(\mathbf{p})) \ln(1-n(\mathbf{p}))] \frac{d\mathbf{p}}{(2\pi)^3} \quad (2)$$

which follows from the combinatorial reasoning. Since the entropy of the superconducting ground state is zero, it follows from Eq. (2) that the entropy is discontinuous at the phase transition point, with its discontinuity $\Delta S = S_0$. The latent heat q of the transition from the asymmetric to the symmetric phase is $q = T_c S_0 = 0$ since $T_c = 0$. Because of the stability condition at the point of the first-order phase transition, we have $\Phi_0[n(\mathbf{p})] = \Phi[\kappa(\mathbf{p})]$. Obviously, the condition is satisfied since $q = 0$.

At $T = 0$, a quantum phase transition is driven by a nonthermal control parameter, e.g. the number density x . To clarify the role of x , consider the effective mass M^*

which is related to the bare electron mass m by the well-known Landau equation [26] which is also valid, when M^* strongly depends on B , T , or x [16]:

$$\frac{1}{M^*} = \frac{1}{m} + \int \frac{\mathbf{p}_F \mathbf{p}_1}{p_F^3} F(\mathbf{p}_F, \mathbf{p}_1) \frac{\partial n(p_1, T)}{\partial p_1} \frac{d\mathbf{p}_1}{(2\pi)^3}. \quad (3)$$

Here, we omit the spin indices for simplicity, $n(\mathbf{p}, T)$ is quasiparticle occupation number, and F is the Landau amplitude. At $T = 0$, Eq. (3) reads [27, 28]

$$\frac{M^*}{m} = \frac{1}{1 - N_0 F^1(x)/3}. \quad (4)$$

Here, N_0 is the density of states of the free electron gas, and $F^1(x)$ is the p -wave component of the Landau interaction amplitude F . When $x = x_c$ at some quantum critical point (QCP), $F^1(x)$ achieves a certain threshold value, and the denominator in Eq. (4) tends to zero so that the effective mass diverges at $T = 0$ [27, 28]. It follows from Eq. (4) that, beyond the QCP $x = x_c$, the effective mass becomes negative. To avoid the unstable and physically meaningless state with a negative effective mass, the system must undergo a quantum phase transition at QCP $x = x_c$ defined by Eq. (1) and which is FCQPT [8, 9, 12, 13].

The schematic phase diagram of the system which is driven to FC by variation of x is reported in Fig. 1. Upon approaching the critical density x_c , the system remains in the LFL region at sufficiently low temperatures [12, 13], which is shown by the shadow area. At QCP x_c shown by the arrow in Fig. 1, the system demonstrates the NFL behavior down to the lowest temperatures. Beyond QCP at finite temperatures, the behavior is remaining the NFL one and is determined by the temperature-independent entropy S_0 [24]. In that case as $T \rightarrow 0$, the system is approaching a quantum critical line (shown by the vertical arrow and the dashed line in Fig. 1) rather than a quantum critical point. Upon reaching the quantum critical line from the above at $T \rightarrow 0$, the system undergoes the first-order quantum phase transition which is FCQPT taking place at $T_c = 0$.

At $T > 0$, the NFL state above the critical line, see Fig. 1, is strongly degenerated. Therefore, it is captured by the other states such as the superconducting (for example, by the superconducting state in CeCoIn₅ [23, 29, 30]) or by an AF state (e.g., the AF one in YbRh₂Si₂ [16, 21, 31]) lifting the degeneracy. The application of a magnetic field $B > B_{c0}$ restores the LFL behavior, where B_{c0} is a critical magnetic field such that the system is driven toward its LFL regime at $B > B_{c0}$ [21, 30, 31]. In some cases, for example in HF metal

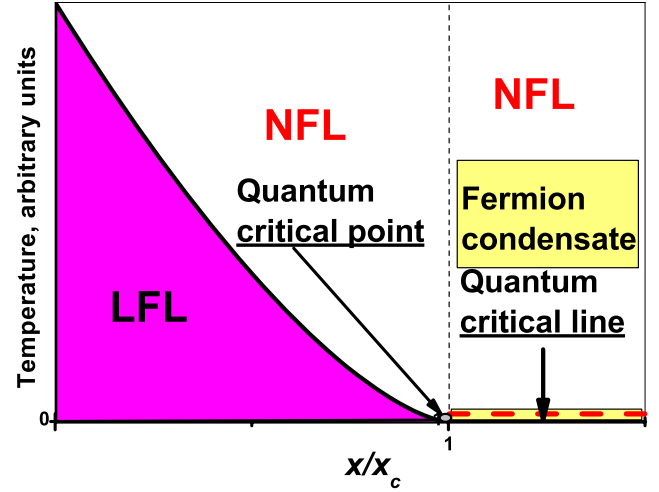


Fig. 1. Schematic phase diagram of the system driven to the FC state. The number density x is taken as the control parameter and depicted as x/x_c . The quantum critical point (QCP), $x/x_c = 1$, of FCQPT is shown by the arrow. At $x/x_c < 1$ and sufficiently low temperatures, the system is in the Landau Fermi liquid (LFL) state as shown by the shadow area. At $T = 0$ and beyond QCP, $x/x_c > 1$, the system is at the quantum critical line depicted by the dash line and shown by the vertical arrow. The critical line is characterized by the FC state with a finite superconducting order parameter κ . At any finite temperature, the order parameter κ is destroyed, and the entropy becomes discontinuous at $T_c = 0$, the system undergoes the first-order phase transition and exhibits the NFL behavior at $T > 0$

CeRu₂Si₂, $B_{c0} = 0$ (see, e.g., [32]), while $B_{c0} \simeq 0.06$ T in YbRh₂Si₂ [21, 31]. In our simple model, B_{c0} is taken as a parameter.

3. Scaling Behavior of the Effective Mass

The schematic phase diagram of the HF metal YbRh₂Si₂ is presented in Fig. 2. A magnetic field B is taken as the control parameter. The FC state and the region lying at $x/x_c \geq 1$ (see Fig. 1) can be captured by the superconducting, ferromagnetic, antiferromagnetic (AF), etc. states lifting the degeneracy [12, 13]. Since we consider the HF metal YbRh₂Si₂, the AF state takes place [21, 31], as shown in Fig. 2. As seen from Fig. 2, at elevated temperatures and a fixed magnetic field, the NFL regime occurs, while rising B again drives the system from the NFL region to the LFL one. Below, we consider the transition region when the system moves from the NFL regime to the LFL one along the dash-dot horizontal arrow at rising B , and it moves from the LFL regime to the NFL one along the solid vertical arrow at rising T .

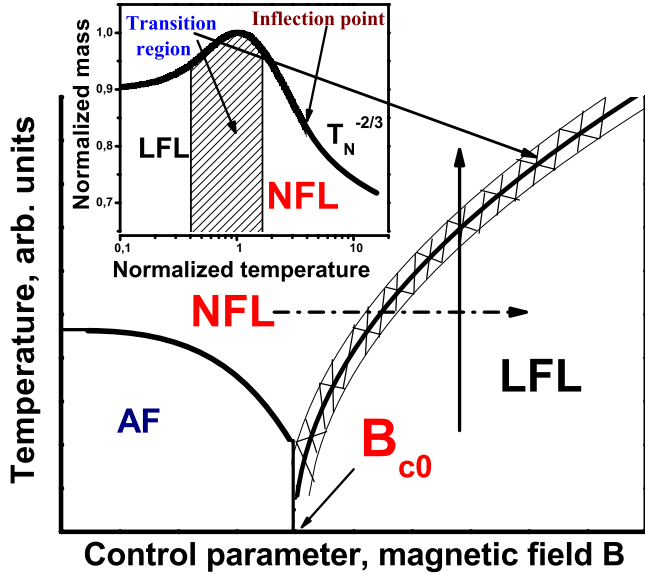


Fig. 2. Schematic phase diagram of the HF metal YbRh_2Si_2 . AF denotes antiferromagnetic state. At $T = 0$, B_{c0} is the magnetic field, at which the effective mass diverges, and the AF state vanishes. At $B > B_{c0}$, the system is in its paramagnetic state. The vertical arrow shows the transition from the LFL regime to the NFL one at fixed B along T with M^* depending on T . The dash-dot horizontal arrow illustrates the system moving from the NFL regime to the LFL one along B at fixed T . The inset shows a schematic plot of the scaling behavior of the normalized effective mass versus the normalized temperature. The transition regime, where M_N^* reaches its maximum value M_M^* at $T = T_M$, is shown by the hatched area both in the main panel and in the inset. The arrows mark the position of the inflection point in M_N^* and the transition region

To explore a scaling behavior of M^* , we write the quasiparticle distribution function as $n_1(\mathbf{p}) = n(\mathbf{p}, T) - n(\mathbf{p})$, with $n(\mathbf{p})$ is the step function, and Eq. (3) then becomes

$$\frac{1}{M^*(T)} = \frac{1}{M^*} + \int \frac{\mathbf{p}_F \mathbf{p}_1}{p_F^3} F(\mathbf{p}_F, \mathbf{p}_1) \frac{\partial n_1(p_1, T)}{\partial p_1} \frac{d\mathbf{p}_1}{(2\pi)^3}. \quad (5)$$

At QCP, the effective mass M^* diverges, and Eq. (5) becomes homogeneous determining M^* as a function of the temperature

$$M^*(T) \propto T^{-2/3}, \quad (6)$$

while the system exhibits the NFL behavior [12, 15]. If the system is located before QCP, M^* is finite. At low temperatures, the system demonstrates the LFL behavior, i.e. $M^*(T) \simeq M^* + a_1 T^2$, with a_1 being a constant

(see the inset to Fig. 2). Obviously, the LFL behavior takes place when the second term on the right-hand side of Eq. (5) is small in comparison with the first one. Then, at rising temperatures, the system enters the transition regime: M^* grows, reaching its maximum M_M^* at $T = T_M$, with the subsequent diminishing. Near temperatures $T \geq T_M$, the last “traces” of the LFL regime disappear, the second term starts to dominate. Equation (5) becomes homogeneous again, and the NFL behavior restores, manifesting itself in decreasing M^* as $T^{-2/3}$, see Eq. (6). When the system is near QCP, it turns out that the solution of Eq. (5) $M^*(T)$ can be well approximated by a simple universal interpolating function [12, 15, 30]. The interpolation occurs between the LFL ($M^* \simeq M^* + a_1 T^2$) and NFL ($M^* \propto T^{-2/3}$) regimes, thus describing the above crossover [12, 15]. Introducing the dimensionless variable $y = T_N = T/T_M$, we obtain the desired expression

$$M_N^*(y) \approx c_0 \frac{1 + c_1 y^2}{1 + c_2 y^{8/3}}. \quad (7)$$

Here, $M_N^* = M^*/M_M^*$ is the normalized effective mass, and $c_0 = (1 + c_2)/(1 + c_1)$, c_1 , and c_2 are the fitting parameters parametrizing the Landau amplitude.

The inset to Fig. 2 demonstrates the scaling behavior of the normalized effective mass $M_N^* = M^*/M_M^*$ versus the normalized temperature $T_N = T/T_M$, where M_M^* is the maximum value reached by M^* at $T = T_M$. At $T \ll T_M$, the LFL regime takes place. At $T \gg T_M$, the $T^{-2/3}$ regime takes place. This is marked as the NFL one, since the effective mass depends strongly on the temperature. The temperature region $T \simeq T_M$ signifies the transition between the LFL regime with almost constant effective mass and the NFL behavior given by $T^{-2/3}$ dependence. Thus, the temperatures $T \sim T_M$ can be regarded as the transition region between the LFL and NFL regimes. The transition temperatures are not really a phase transition. These necessarily are broad, very much depending on the criteria for determination of the point of such a transition, as it is seen from the inset to Fig. 2. As usual, the transition temperature is extracted from the temperature dependence of charge transport, for example, from the resistivity $\rho(T) = \rho_0 + AT^2$, where ρ_0 is the residual resistivity, and A is the LFL coefficient. The crossover takes place at temperatures, where the resistance starts to deviate from the LFL T^2 behavior. Obviously, the measure of the deviation from the LFL T^2 behavior cannot be defined unambiguously. Therefore, different measures produce different results.

It is possible to transport Eq. (5) to the case of the application of magnetic fields [12, 15, 30]. The application of a magnetic field restores the LFL behavior, so that M_M^* depends on B as

$$M_M^* \propto (B - B_{c0})^{-2/3}, \quad (8)$$

while

$$T_M \propto \mu_B (B - B_{c0}), \quad (9)$$

where μ_B is the Bohr magneton [12, 15, 30]. Employing Eqs. (8) and (9) to calculate M_M^* and T_M , we conclude that Eq. (7) is valid to describe the normalized effective mass in external fixed magnetic fields with $y = T/(B - B_{c0})$. On the other hand, Eq. (7) is valid when the applied magnetic field becomes a variable, while the temperature is fixed $T = T_f$. In that case, as seen from Eqs. (6), (7), and (8), it is convenient to rewrite the variable as $y = (B - B_{c0})/T_f$ and Eq. (9) as

$$\mu_B (B_M - B_{c0}) \propto T_f. \quad (10)$$

It follows from Eq. (7) that, in contrast to the Landau paradigm of quasiparticles, the effective mass strongly depends on T and B . As we will see, it is this dependence that forms the NFL behavior. It follows also from Eq. (7) that a scaling behavior of M^* near QCP is determined by the absence of appropriate external physical scales to measure the effective mass and the temperature. At fixed magnetic fields, the characteristic scales of the temperature and of the function $M^*(T, B)$ are defined by both T_M and M_M^* , respectively. At fixed temperatures, the characteristic scales are $(B_M - B_{c0})$ and M_M^* . It follows from Eqs. (8) and (9) that, at fixed magnetic fields, $T_M \rightarrow 0$, and $M_M^* \rightarrow \infty$, and the width of the transition region shrinks to zero as $B \rightarrow B_{c0}$, when these are measured on the external scales. In the same way, it follows from Eqs. (6) and (10) that, at fixed temperatures, $(B_M - B_{c0}) \rightarrow 0$, and $M_M^* \rightarrow \infty$, and the width of the transition region shrinks to zero as $T_f \rightarrow 0$. Thus, the application of the external scales obscures the scaling behavior of the effective mass and of the thermodynamic and transport properties.

A few remarks are in order here. As we shall see, the magnetic field dependences of the effective mass or some other observable like the longitudinal magnetoresistance do not have ‘‘peculiar points’’ like maximum. The normalization are to be performed at the other points like the inflection point at $T = T_{\text{inf}}$ (or at $B = B_{\text{inf}}$) shown in the inset to Fig. 2 by the arrow. Such a normalization is possible, since it is established on the internal scales, $T_{\text{inf}} \propto T_M \propto (B - B_{c0})$.

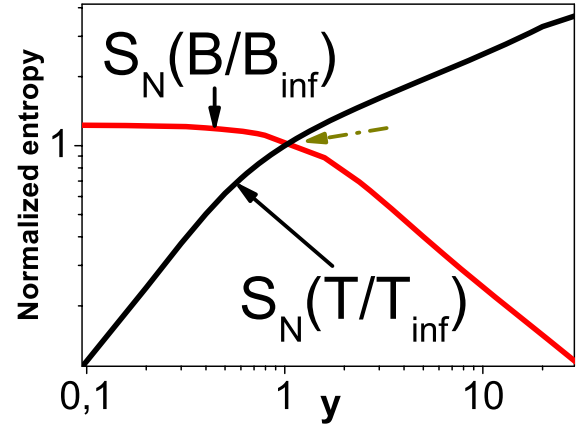


Fig. 3. Normalized entropy $S_N(B/B_{\text{inf}})$ versus $y = B/B_{\text{inf}}$ and the normalized entropy $S_N(T/T_{\text{inf}})$ versus $y = T/T_{\text{inf}}$ calculated at a fixed temperature and a fixed magnetic field, respectively, are represented by the solid lines and shown by the arrows. The inflection point is depicted by the dash-dot arrow

4. NFL Behavior of the HF Metal YbRh_2Si_2

In what follows, we compute the effective mass and employ Eq. (7) for estimations of considered values. To compute the effective mass $M^*(T, B)$, we solve Eq. (5) with a special form of the Landau interaction amplitude, see [12, 15] for details. The choice of the amplitude is dictated by the fact that the system has to be at QCP, which means that the first two p -derivatives of the single-particle spectrum $\varepsilon(\mathbf{p})$ should equal zero. Since the first derivative is proportional to the reciprocal quasiparticle effective mass $1/M^*$, its zero just signifies QCP of FCQPT. A zero of the second derivative means that the spectrum $\varepsilon(\mathbf{p})$ has an inflection point at p_F rather than a maximum. Thus, the lowest term of the Taylor expansion of $\varepsilon(\mathbf{p})$ is proportional to $(p - p_F)^3$ [15]. After the solution of Eq. (5), the obtained spectrum had been used to calculate the entropy $S(B, T)$, which had been recalculated, in turn, to the effective mass $M^*(T, B)$ by virtue of the well-known LFL relation $M^*(T, B) = S(T, B)/T$. The results of our calculations of the normalized entropy as a function of the normalized magnetic field $B/B_{\text{inf}} = y$ and as a function of the normalized temperature $y = T/T_{\text{inf}}$ are given in Fig. 3. Here, T_{inf} and B_{inf} are the corresponding inflection points of the function S . We normalize the entropy by its value at the inflection point $S_N(y) = S(y)/S(1)$. As seen from Fig. 3, our calculations corroborate the scaling behavior of the normalized entropy. That is, the curves at different temperatures and magnetic fields merge into the single one in terms of the variable y . The

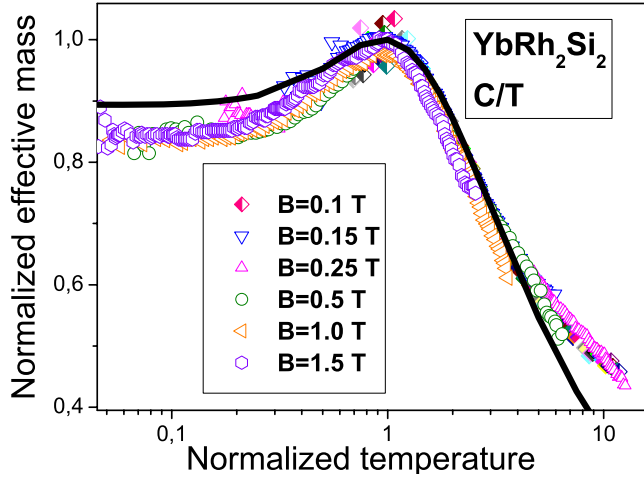


Fig. 4. Normalized effective mass M_N^* extracted from the measurements of the specific heat C/T on YbRh_2Si_2 in magnetic fields B [19] listed in the legend. The results of our calculations are depicted by the solid curve tracing the scaling behavior of M_N^*

inflection point T_{inf} in $S(T)$ makes $M^*(T, B)$ have its maximum as a function of T , while $M^*(T, B)$ versus B has no maximum. We note that our calculations of the entropy confirm the validity of Eq. (7) and the scaling behavior of the normalized effective mass.

4.1. Heat capacity

Exciting measurements of $C/T \propto M^*$ on samples of the new generation of YbRh_2Si_2 in different magnetic fields B up to 1.5 T [19] allow us to identify the scaling behavior of the effective mass M^* and to observe the different regimes of M^* behavior such as the LFL regime, transition region from the LFL to the NFL regimes, and the NFL regime itself. A maximum structure in $C/T \propto M_M^*$ at T_M appears under the application of a magnetic field B , and T_M shifts to higher T , as B is increased. The value of $C/T = \gamma_0$ is saturated toward lower temperatures, by decreasing at the increasing magnetic field, where γ_0 is the Sommerfeld coefficient [19].

The transition region corresponds to the temperatures, where the vertical arrow in the main panel of Fig. 2 crosses the hatched area. The region width proportional to $T_M \propto (B - B_{c0})$ shrinks, T_M moves to the zero temperature, and $\gamma_0 \propto M^*$ increases as $B \rightarrow B_{c0}$. These observations are in accord with the facts [19].

To obtain the normalized effective mass M_N^* , the maximum structure in C/T was used to normalize C/T , and T was normalized by T_M . In Fig. 4, M_N^* as a function of the normalized temperature T_N is shown by geometrical figures, our calculations are shown by the solid

line. Figure 4 reveals the scaling behavior of the normalized experimental curves, and the scaled curves at different magnetic fields B merge into the single one in terms of the normalized variable $y = T/T_M$. As seen, the normalized mass M_N^* extracted from the measurements is not a constant, as it would be for LFL. The two regimes (the LFL regime and the NFL one) separated by the transition region, as depicted by the hatched area in the inset to Fig. 2, are clearly seen in Fig. 4 illuminating a good agreement between the theory and the facts. It is worth noting that the normalization procedure allows us to construct the scaled function C/T extracted from the facts in a wide range of variation of the normalized temperature. Indeed, it integrates measurements of C/T taken at the application of different magnetic fields into the unique function which demonstrates the scaling behavior over three decades in the normalized temperature as seen from Fig. 4.

4.2. Magnetization

Consider now the magnetization M as a function of the magnetic field B at a fixed temperature $T = T_f$,

$$M(B, T) = \int_0^B \chi(b, T) db, \quad (11)$$

where the magnetic susceptibility χ is given by [26]

$$\chi(B, T) = \frac{\beta M^*(B, T)}{1 + F_0^a}. \quad (12)$$

Here, β is a constant, and F_0^a is the Landau amplitude related to the exchange interaction [26]. In the case of strongly correlated systems, $F_0^a \geq -0.9$ [27, 28]. Therefore, as seen from Eq. (12), the coefficients β and $(1 + F_0^a)$ drop out from the result due to the normalization, and $\chi \propto M^*$.

One might suppose that F_0^a can strongly depend on B . This is not the case, since the Kadowaki–Woods ratio is conserved [31, 33–35], $A(B)/\gamma_0^2(B) \propto A(B)/\chi^2(B) \propto \text{const}$, we have $\gamma_0 \propto M^* \propto \chi$. Here, A is the coefficient in the T^2 dependence of the resistivity ρ .

Our calculations show that the magnetization exhibits a kink at some magnetic field $B = B_k$. The experimental magnetization demonstrates the same behavior [20]. We use B_k and $M(B_k)$ to normalize B and M , respectively. The normalized magnetization $M(B)/M(B_k)$ extracted from facts [20] depicted by the geometrical figures and the calculated magnetization shown by the solid line are

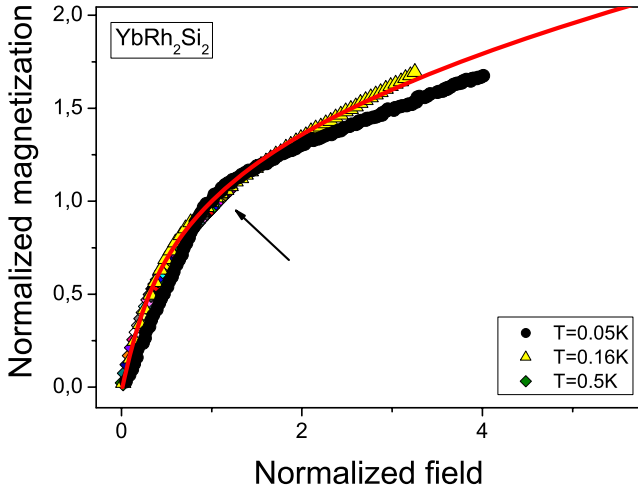


Fig. 5. Field dependences of the normalized magnetization M collected at different temperatures shown at the right bottom corner are extracted from measurements collected on YbRu_2Si_2 [20]. The kink (shown by the arrow) is clearly seen at the normalized field $B_N = B/B_k \simeq 1$. The solid curve represents our calculations

presented in Fig. 5. As seen, the scaled data at different T_f merge into the single one in terms of the normalized variable $y = B/T_k$. It is also seen that these exhibit the energy scales separated by a kink at the normalized magnetic field $B_N = B/B_k = 1$. The kink is a crossover point from the fast to slow growth of M at a rising magnetic field. It is seen from Fig. 5 that our calculations are in good agreement with the facts, and all the data exhibit the kink (shown by the arrow) at $B_N \simeq 1$ taking place as soon as the system enters the transition region corresponding to the magnetic fields, where the horizontal dash-dot arrow in the main panel of Fig. 2 crosses the hatched area. Indeed, as seen from Fig. 5, M is a linear function of B at lower magnetic fields, since M^* is approximately independent of B . Then, it follows from Eqs. (7) and (8) that, at elevated magnetic fields, M^* becomes a diminishing function of B and generates the kink in $M(B)$ separating the energy scales discovered in [18, 20]. Then, as seen from Eq. (10), the magnetic field B_k , at which the kink appears, $B_k \simeq B_M \propto T_f$, shifts to lower B , as T_f is decreased. This observation is in accord with the facts [18, 20].

4.3. Longitudinal magnetoresistance

Consider the longitudinal magnetoresistance (LMR) $\rho(T, B) = \rho_0 + A(T, B)T^2$ as a function of B at fixed $T = T_f$. In that case, the classical contribution to LMR due to the orbital motion of carriers induced by the Lorentz force is small, while the Kadowaki–Woods

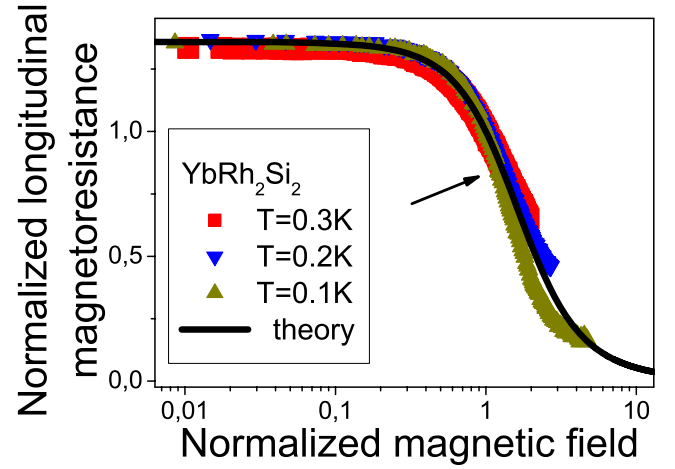


Fig. 6. Magnetic field dependence of the normalized magnetoresistance ρ_N versus the normalized magnetic field. ρ_N was extracted from LMR of YbRh_2Si_2 at different temperatures [18, 20] listed in the legend. The inflection point is shown by the arrow, and the solid line represents our calculations

relation [31, 33–35], $K = A/\gamma_0^2 \propto A/\chi^2 = \text{const}$, allows us to employ M^* to construct the coefficient A [36], since $\gamma_0 \propto \chi \propto M^*$. As a result, $\rho(T, B) - \rho_0 \propto (M^*)^2$. Figure 6 shows the normalized magnetoresistance

$$\rho_N(y) = \frac{\rho(y) - \rho_0}{\rho_{\text{inf}}} \propto (M_N^*(y))^2 \quad (13)$$

versus the normalized magnetic field $y = B/B_{\text{inf}}$ at different temperatures shown in the legend. Here, ρ_{inf} and B_{inf} are the LMR and the magnetic field, respectively, taken at the inflection point marked by the arrow in Fig. 6. Both theoretical (shown by the solid line) and experimental (marked by the geometrical figures) curves have been normalized by their inflection points, which also reveals the scaling behavior. The scaled curves at different temperatures merge into the single one as a function of the variable y and show the scaling behavior over three decades in the normalized magnetic field. The transition region, at which LMR starts to decrease, is shown in the inset to Fig. 2 by the hatched area. Obviously, as seen from Eq. (10), the width of the transition region being proportional to $B_M \simeq B_{\text{inf}} \propto T_f$ decreases as the temperature T_f is lowered. In the same way, the inflection point of LMR, generated by the inflection point of M^* shown in the inset to Fig. 2 by the arrow, shifts to lower B , as T_f is decreased. All these observations are in excellent agreement with the facts [18, 20].

It is instructive to demonstrate that the same effective mass employed to calculate LMR shown in Fig. 6 gives good description of the magnetoresistance (MR)

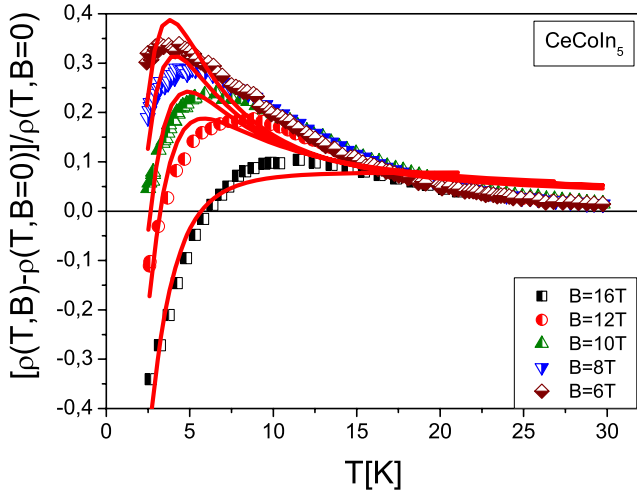


Fig. 7. MR versus the temperature T as a function of the magnetic field B . The experimental data on MR were collected on CeCoIn_5 at a fixed magnetic field B [37] shown in the right bottom corner of the figure. The solid lines represent our calculations

collected in measurements on CeCoIn_5 . Figure 7 shows the calculated MR versus the temperature T as a function of the magnetic field B together with the experimental points from [37]. We note that both the classical contributions to MR due to the orbital motion of carriers induced by the Lorentz force and ρ_0 were omitted. As seen from Fig. 7, our description of the experiment is pretty good [38].

4.4. Magnetic entropy

The evolution of the magnetic entropy derivative $dS(B, T)/dB$ as a function of the magnetic field B at a fixed temperature T_f is of great importance, since it allows us to study the scaling behavior of the derivative of the effective mass $TdM^*(B, T)/dB \propto dS(B, T)/dB$, while the scaling properties of the effective mass $M^*(B, T)$ can be analyzed via LMR (see Fig. 6).

As seen from Eqs. (7) and (10), at $y \leq 1$, the derivative $-dM_N(y)/dy \propto y$ with $y = (B - B_{c0})/(B_{\text{inf}} - B_{c0}) \propto (B - B_{c0})/T_f$. We note that the effective mass as a function of B does not have maximum. At elevated y , the derivative $-dM_N(y)/dy$ possesses a maximum at the inflection point and then becomes a diminishing function of y . Upon using the variable $y = (B - B_{c0})/T_f$, we conclude that, at decreasing temperatures, the leading edge of the function $-dS/dB \propto -TdM^*/dB$ becomes steeper, and its maximum at $(B_{\text{inf}} - B_{c0}) \propto T_f$ is higher. These observations are in quantitative

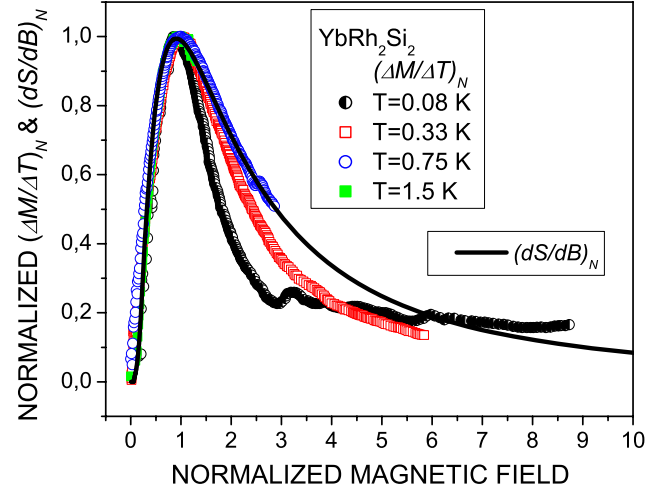


Fig. 8. Normalized magnetization difference divided by the temperature increment $(\Delta M/\Delta T)_N$ versus the normalized magnetic field at fixed temperatures listed in the legend is extracted from the facts collected on YbRh_2Si_2 [21]. The results of our calculations of the normalized derivative $(dS/dB)_N \simeq (\Delta M/\Delta T)_N$ versus the normalized magnetic field are shown by the solid line

agreement with striking measurements of the magnetization difference divided by the temperature increment, $-\Delta M/\Delta T$, as a function of the magnetic field at fixed temperatures T_f collected on YbRh_2Si_2 [21]. We note that, according to the well-known thermodynamic equality, $dM/dT = dS/dB$ and $\Delta M/\Delta T \simeq dS/dB$. To carry out a quantitative analysis of the scaling behavior of $-dM^*(B, T)/dB$, we calculate the normalized entropy S shown in Fig. 3 as a function of B/B_{inf} at a fixed temperature T_f . Figure 8 demonstrates the normalized $(dS/dB)_N$ as a function of the normalized magnetic field. The scaled function $(dS/dB)_N$ is obtained by normalizing $(-dS/dB)$ by its maximum taking place at B_M , and the field B is scaled by B_M . The measurements of $-\Delta M/\Delta T$ are normalized in the same way and depicted in Fig. 8 as $(\Delta M/\Delta T)_N$ versus the normalized field. It is seen from Fig. 8 that our results shown by the solid line are in good agreement with the facts, and the scaled functions $(\Delta M/\Delta T)_N$ extracted from the facts show the scaling behavior in a wide range of variation of the normalized magnetic field B/B_M .

4.5. Energy scales and $T - B$ phase diagram for YbRh_2Si_2

Figure 9 shows T_{inf} and T_M versus B depicted by the solid and dash-dotted lines, respectively. The boundary between the NFL and LFL regimes is shown by

the dashed line, and AF marks the antiferromagnetic state. The corresponding data are taken from [18–20,31]. It is seen that our calculations are in good agreement with the facts [17]. In Fig. 9, the solid and dash-dotted lines corresponding to the functions T_{inf} and T_M , respectively, represent the positions of the kinks separating the energy scales in C and M reported in [18, 20]. It is seen that our calculations are in accord with facts, and we conclude that the energy scales are reproduced by Eqs. (9) and (10) and related to the peculiar points of the normalized effective mass M_N^* . The points are the inflection point T_{inf} and the maximum point T_M , at which the transition region is located. These are shown by the arrows in the inset to Fig. 2.

At $B \rightarrow B_{c0}$, both $T_{\text{inf}} \rightarrow 0$ and $T_M \rightarrow 0$. Thus, the LFL and the transition regimes of both C/T and M , as well as these of LMR and the magnetic entropy, are shifted to very low temperatures. Therefore, due to experimental difficulties, these regimes cannot be often observed in experiments on HF metals. As is seen from Figs. 4, 5, 6, 8, and 9, the normalization allows us to construct the unique scaled thermodynamic and transport functions extracted from the experimental facts in a wide range of variation of the scaled variable y . As seen from the above-mentioned figures, the constructed normalized thermodynamic and transport functions show the scaling behavior over three decades in the normalized variable.

5. Universal Behavior of Two-Dimensional ^3He at Low Temperatures

The bulk liquid ^3He is historically the first object, to which the Landau Fermi-liquid (LFL) theory had been applied [26]. This substance, being an intrinsically isotropic Fermi liquid with the negligible spin-orbit interaction is ideal to test the LFL theory. It is remarkable that the same ^3He becomes the first 2D homogeneous Fermi liquid, in which the NFL behavior was detected [39–41]. 2D ^3He has a very important feature: a change of the number density x of a ^3He film drives it toward QCP, at which the quasiparticle effective mass M^* diverges [39–41]. This peculiarity allows one to plot the experimental temperature-density phase diagram which can be directly compared with the theoretical phase diagram shown in Fig. 1. As a result, 2D ^3He becomes an ideal system to test a theory describing the NFL behavior. Namely, the neutral atoms of ^3He are fermions interacting with one another by van-der-Waals forces with

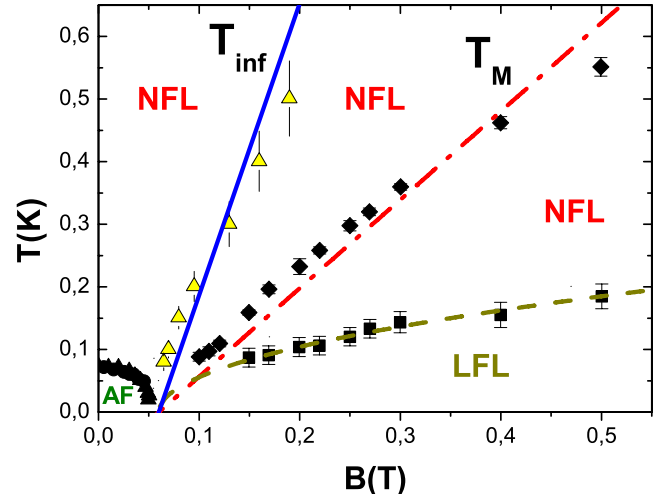


Fig. 9. $T - B$ phase diagram for YbRh_2Si_2 . Solid circles represent the boundary between AF and NFL states. The solid squares denote the boundary of the NFL and LFL regimes [18, 20, 31] shown by the dotted line which is approximated by $\sqrt{B - B_{c0}}$ [12]. Diamonds mark the maxima T_M of C/T [19] shown in Fig. 2. The dash-dot line is approximated by $T_M \propto a(B - B_{c0})$, a is a fitting parameter, see Eq. (9). Triangles along the solid line denote T_{inf} in LMR [18, 20] shown in Fig. 5, the solid line represents the function $T_{\text{inf}} \propto b(B - B_{c0})$, where b is a fitting parameter, see Eq. (10)

a strong hardcore repulsion and a weakly attractive tail. The different character of the interparticle interaction along with the fact that the mass of ^3He atom is 3 orders of magnitude larger than that of an electron makes ^3He systems to have drastically different properties than those of HF metals. Because of this difference, nobody can be sure that the macroscopic physical properties of these systems will be more or less similar to each other at their QCP.

In this section, we show that, in spite of very different microscopic nature of 2D ^3He and 3D HF metals, their main universal features at their QCP are the same, being dictated by the extended quasiparticles paradigm. Our analysis of the experimental measurements has shown that the behavior of 2D ^3He is quite similar to that of HF compounds with various ground state magnetic properties. Namely, we demonstrate that the main universal features of the ^3He experimental $T-x$ phase diagram resemble those of HF metals and can be well captured, by utilizing the notion of FCQPT embracing the extended quasiparticles paradigm and thus by deriving NFL properties of above systems from the paradigm. We also show that the universal behavior of the effective mass of 2D ^3He coincides with that observed in HF metals.

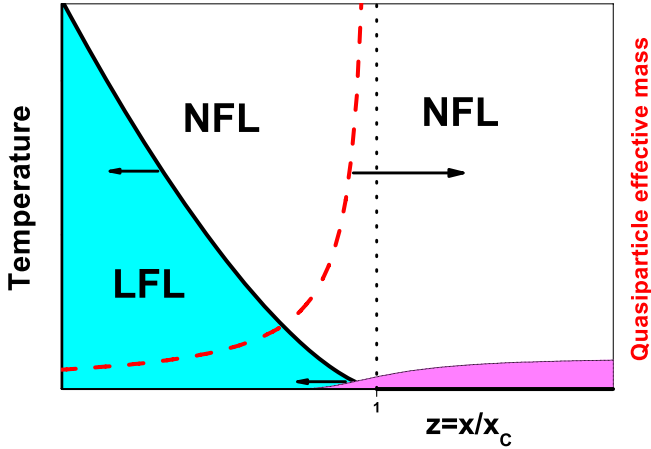


Fig. 10. Temperature-number density phase diagram of 2D ^3He . The part for $z < 1$ corresponds to the HF behavior divided into the LFL and NFL parts by the line $T_M(z) \propto (1-z)^{3/2}$, where T_M is the effective mass maximum temperature. The exponent $3/2 = 1.5$ coming from Eq. (15) is in good agreement with the experimental value of 1.7 ± 0.1 [39]. The dependence $M^*(z) \propto (1-z)^{-1}$ shown by the dashed line points out QCP taking place at $z = 1$. The regime for $z \geq 1$ consists of the LFL piece (the shadowed region beginning in the intervening phase $z \leq 1$ [39], which is due to the substrate inhomogeneities, see the text) and the NFL regime at higher temperatures

5.1. The temperature-number density phase diagram of 2D ^3He

As we have seen in Section I, at QCP $x = x_c$, the effective mass diverges at $T = 0$, and the leading term of this divergence given by Eq. (4) reads

$$\frac{M^*(x)}{M} = A + \frac{B}{1-z}, \quad z = \frac{x}{x_c}. \quad (14)$$

Equation (14) is valid in both 3D and 2D cases, while the values of factors A and B depend on the dimensionality and the interparticle interaction [12]. At $x > x_c$, the fermion condensation takes place. Here, we confine ourselves to the case $x < x_c$.

Equation (14) shows that the maximum value of the effective mass $M_M^* \propto 1/(1-z)$, and it follows from (6) that $M_M^* \propto T^{-2/3}$. As a result, we obtain that T_M , at which the effective mass reaches its maximum value $M_M^* \propto T^{-2/3}$, is given by

$$T_M \propto (1-z)^{3/2}. \quad (15)$$

We note that the obtained results are in agreement with numerical calculations [12, 15].

In Fig. 10, we show the phase diagram of 2D ^3He in the variables $T-z$ (see Eq. (14)). For the sake of comparison, the plot of the effective mass versus z is shown by a

dashed line. The dependence $M^*(z) \propto (1-z)^{-1}$ demonstrates that the effective mass diverges at QCP with $z = 1$ in accordance with the general phase diagram displayed in Fig. 1. The part of the diagram, where $z < 1$, corresponds to the HF behavior and consists of LFL and NFL parts divided by the line $T_M(z) \propto (1-z)^{3/2}$. We draw attention that our exponents 1 (see Eq. (14)) and $3/2 = 1.5$ (see Eq. (15)) are in good agreement with those from [39]. The good coincidence between the theoretical and experimental exponents favors the realization of our FCQPT scenario in the NFL behavior of both 2D ^3He and HF metals, as the former system is similar in great details to them.

The regime for $z > 1$ located above the quantum critical line, see Figs. 10 and 1, consists of the low-temperature LFL piece, (shown in Fig. 10 by the shadowed region beginning in the intervening phase $z \leq 1$ [39]) and the NFL regime at higher temperatures. The former LFL piece is related to the peculiarities of a substrate, on which 2D ^3He film is placed. Namely, it is related to the weak substrate heterogeneity (steps and edges on its surface), so that quasiparticles, being localized (pinned) on it, give rise to the LFL behavior [39, 40]. That is, the peculiarities of the substrate eliminate the degeneracy generated by the FC state taking place at $z > 1$ in the same way as the AF state does in the case of YbRh_2Si_2 , see Fig. 2. At elevated temperatures, the competition between the thermal and pinning energies returns the system back to the unpinned state restoring the NFL behavior. As HF metals do not have a substrate, the LFL behavior is induced by the AF state lifting the degeneracy. At elevated temperatures, this state is destroyed and exhibits the NFL behavior, as is shown in Fig. 2. If the AF state were absent and some disorder (like point defects, dislocations, etc.) were present in the lattice, a rather thin LFL piece could take place at low temperatures.

5.2. NFL behavior of 2D ^3He versus that of HF metals

As we have seen above, $M^*(T)$ can be measured in experiments on strongly correlated Fermi systems. For example, $M^*(T) \propto C(T)/T \propto S(T)/T \propto M_0(T) \propto \chi(T)$, where $C(T)$ is the specific heat, $S(T)$ is the entropy, $M_0(T)$ is the magnetization, and $\chi(T)$ is the AC magnetic susceptibility. If the measurements are performed at fixed x , then, as follows from Eq. (7), the effective mass reaches the maximum at $T = T_M$. Upon normalizing both $M^*(T)$ by its peak value at each x and the temperature by T_M , we see from Eq. (7) that, in the

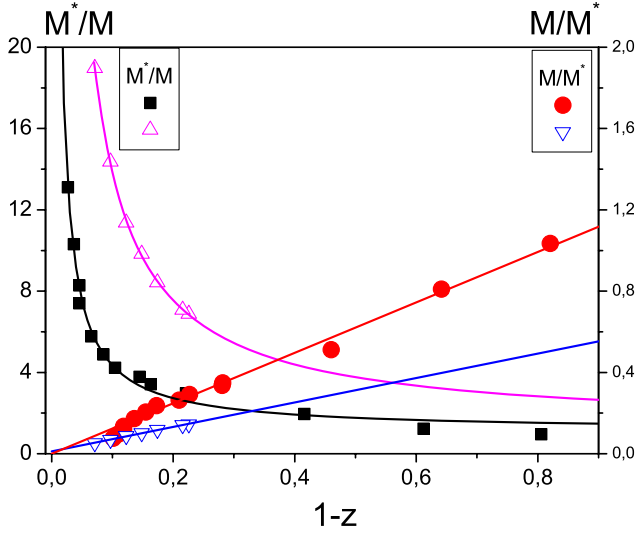


Fig. 11. Dependence of the effective mass $M^*(z)$ on the dimensionless density $1-z = 1-x/x_c$. Experimental data from [41] are shown by circles and squares and those from [39] are shown by triangles. The effective mass is fitted as $M^*(z)/M \propto A+B/(1-z)$ [see Eq. (14)], while the reciprocal one as $M/M^*(z) \propto A_1 z$, where A, B and A_1 are constants

case of 2D ^3He , all the curves also merge into the single one, by demonstrating a scaling behavior.

In Fig. 11, we show the experimental values of effective mass $M^*(z)$ obtained by the measurements on a ^3He monolayer [41]. These measurements, in coincidence with those from [39], show the divergence of the effective mass at $x = x_c$. To show that our FC-QPT approach is able to describe the above data, we represent the fit of $M^*(z)$ by the fractional expression $M^*(z)/M \propto A+B/(1-z)$ and the reciprocal effective mass by the linear fit $M/M^*(z) \propto A_1 z$. We note that the linear fit has been used to describe the experimental data for a bilayer of ^3He [39], and we use this function here for the sake of illustration. It is seen from Fig. 11 that the data [39] (^3He bilayer) can be equally well approximated by both linear and fractional functions, while the data [41] cannot. For instance, both fitting functions give $x_c \approx 9.8 \text{ nm}^{-2}$ for the critical density in a bilayer, while these values are different for a monolayer [41]: $x_c = 5.56$ for a linear fit, and $x_c = 5.15$ for a fractional fit. It is seen from Fig. 11 that a linear fit is unable to properly describe the experiment [41] at small $1-z$ (i.e. near $x = x_c$), while the fractional fit describes the experiment very well. This means that more detailed measurements are necessary in the vicinity of $x = x_c$.

We now apply the universal dependence (7) to fit the experiment not only in 2D ^3He but also in 3D HF met-

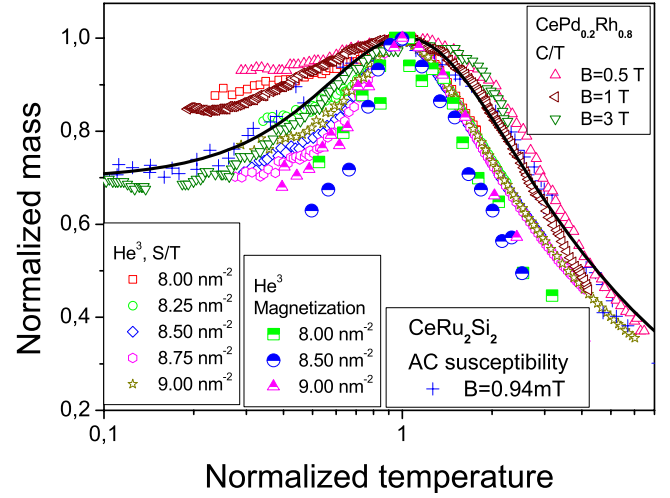


Fig. 12. Normalized effective mass M_N^* as a function of the normalized temperature T/T_M at densities shown in the left bottom corner. The behavior of M_N^* is extracted from experimental data obtained in 2D ^3He [40] and 3D HF compounds with different magnetic ground states such as CeRu_2Si_2 and $\text{CePd}_{1-x}\text{Rh}_x$ [32, 42], fitted by the solid curve given by (7)

als. The quantity $M_N^*(y)$ extracted from measurements of the entropy $S(T)/T$ and the magnetization M_0 on a ^3He film [40] at different densities $x < x_c$ is presented in Fig. 12. In the same figure, the data extracted from the heat capacity of ferromagnet $\text{CePd}_{0.2}\text{Rh}_{0.8}$ [42] and the AC magnetic susceptibility of paramagnet CeRu_2Si_2 [32] are plotted for different magnetic fields. It is seen that the universal behavior of the normalized effective mass given by Eq. (7) and shown by the solid curve is in accord with the experimental facts. All 2D ^3He substances are located at $x < x_c$, where the system progressively disrupts its LFL behavior at elevated temperatures. In that case, the control parameter driving the system toward its QCP x_c is merely the number density x . It is seen that the behavior of $M_N^*(y)$ extracted from $S(T)/T$ and M_0 of 2D ^3He (the entropy $S(T)$ is reported in Fig. S8 A of [40]) looks very much like that of 3D HF compounds. As will be seen from Fig. 14 below, the amplitude and the positions of the magnetization maxima $M_0(T)$ and $S(T)/T$ in 2D ^3He follow nicely Eqs. (14) and (15). We conclude that Eq. (7) allows for the reduction of a 4D function describing the effective mass to a single-variable function. Indeed, the effective mass depends on the magnetic field, temperature, number density, and composition, so that all these parameters can be merged in the single variable by means of an interpolating function like Eq. (7).

The attempt to fit the available experimental data for $C(T)/T$ in 2D ^3He [41] by the universal function $M_N^*(y)$

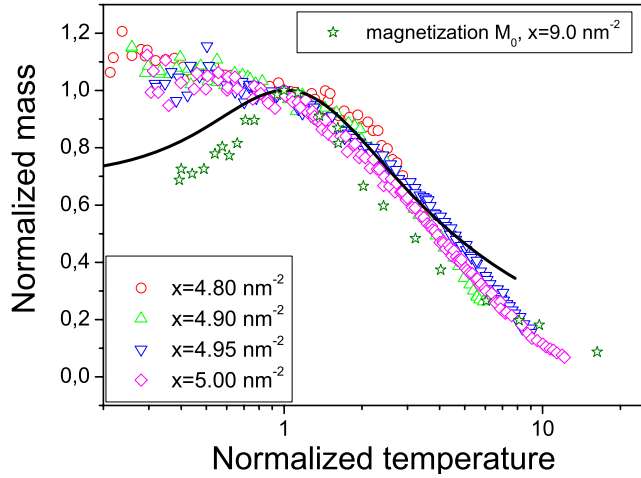


Fig. 13. Dependence $M_N^*(T/T_M)$ at densities shown in the left down corner. The behavior M_N^* is extracted from experimental data for $C(T)/T$ in 2D ^3He [41] and for the magnetization M_0 in 2D ^3He [39]. The solid curve shows the universal function, see the caption to Fig. 12

is demonstrated in Fig. 13. Here, the data extracted from the heat capacity $C(T)/T$ for a ^3He monolayer [41] and the magnetization M_0 for a bilayer [39], are presented. It is seen that the effective mass extracted from these thermodynamic quantities can be well described by the universal interpolation formula (7). We note the qualitative and quantitative similarity between the cases of the double layer [39] and the monolayer [41] of ^3He , as seen from Fig. 13.

In the left panel of Fig. 14, we show the density dependence of T_M , extracted from measurements of the magnetization $M_0(T)$ of a ^3He bilayer [39]. The peak temperature is fitted by Eq. (15). In the same figure, we have also shown the maximal magnetization M_{\max} . It is seen that M_{\max} is well described by the expression $M_{\max} \propto (S/T)_{\max} \propto (1-z)^{-1}$, see Eq. (14). The right panel of Fig. 14 presents the peak temperature T_M and the maximal entropy $(S/T)_{\max}$ versus the number density x . They are extracted from the measurements of $S(T)/T$ on a ^3He bilayer [40]. The fact that both the left and right panels exhibit the same behavior of the curves shows once more that there are indeed the quasi-particles determining the thermodynamic behavior of 2D ^3He near its QCP related to FCQPT.

6. Summary

We have analyzed the non-Fermi liquid behavior of heavy fermion metals and showed that the extended quasiparticles paradigm is strongly valid, while the dependence of

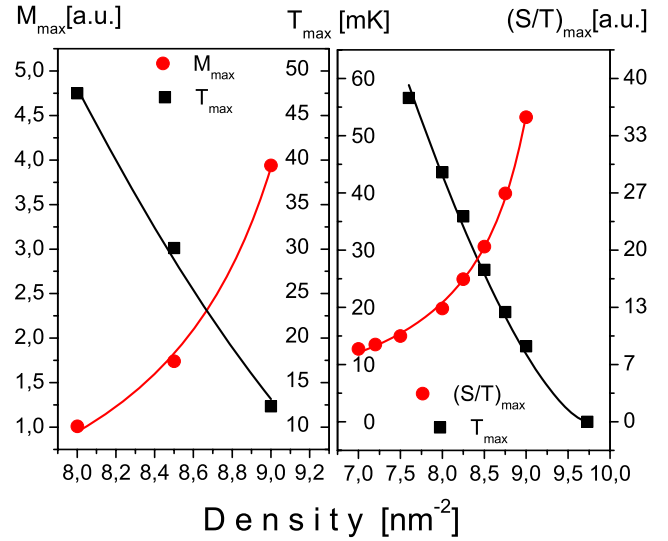


Fig. 14. Left panel, the peak temperatures T_M and the peak values M_{\max} extracted from measurements of the magnetization M_0 in ^3He [39]. Right panel shows T_M and the peak values $(S/T)_{\max}$ extracted from measurements of $S(T)/T$ in ^3He [40]. We approximate $T_M \propto (1-z)^{3/2}$ and $(S/T)_{\max} \propto M_{\max} \propto A/(1-z)$

the effective mass on the temperature, number density, and applied magnetic fields gives rise to the NFL behavior. We have demonstrated that our theoretical study of the heat capacity, magnetization, longitudinal magnetoresistance, and magnetic entropy is in good agreement with the outstanding recent facts collected on the HF metal YbRh_2Si_2 . Our normalization procedure has allowed us to construct the scaled thermodynamic and transport properties in a wide range of variation of the scaled variable. For YbRh_2Si_2 , the constructed thermodynamic and transport functions show the scaling behavior over three decades in the normalized variable. The energy scales in these functions are also explained.

We have described the diverse experimental facts related to the temperature and number density dependences of the thermodynamic characteristics of 2D ^3He by a single universal function of one argument. The above universal behavior is also inherent to HF metals with different magnetic ground states. We obtain the marvellous coincidence with experiment in the framework of our theory. Moreover, these data could be obtained for 2D ^3He only and thus they were inaccessible for analysis in HF metals. This fact also shows the universality of our approach. Thus, we have shown that bringing the experimental data collected on different strongly correlated Fermi systems to the above form immediately reveals their universal scaling behavior. Thus, the theory of fermion condensation quantum phase tran-

sition, preserving the extended quasiparticles paradigm and intimately related to the unlimited growth of the effective mass as a function of the temperature, magnetic field, etc., is capable of describing the strongly correlated Fermi systems.

This work was supported in part by RFBR No. 09-02-00056.

1. G.R. Stewart, *Rev. Mod. Phys.* **73**, 797 (2001).
2. H. v. Löhneysen, A. Rosch, M. Vojta, and P. Wölfle, *Rev. Mod. Phys.* **79**, 1015 (2007).
3. P. Gegenwart, Q. Si, and F. Steglich, *Nature Phys.* **4**, 186 (2008).
4. S. Sachdev, *Nature Phys.* **4**, 173 (2008).
5. P. Coleman and A.J. Schofield, *Nature* **433**, 226 (2005).
6. P. Coleman *et al.*, *J. Phys. Condens. Matter* **13**, R723 (2001).
7. V.A. Khodel, *JETP Lett.* **86**, 721 (2007); V.A. Khodel, J.W. Clark, and M.V. Zverev, arXiv: 0904.1509
8. V.A. Khodel and V.R. Shaginyan, *JETP Lett.* **51**, 553 (1990).
9. M. Ya. Amusia and V.R. Shaginyan, *Phys. Rev. B* **63**, 224507 (2001).
10. J. Dukelsky *et al.*, *Z. Phys. B: Condens. Matter* **102**, 245 (1997).
11. G.E. Volovik, in *Lect. Notes in Physics* **718**, (Springer, Berlin, 2007).
12. V.R. Shaginyan, M.Ya. Amusia, and K.G. Popov, *Physics-Uspokhi* **50**, 563 (2007).
13. V.A. Khodel, J.W. Clark, and M.V. Zverev, *Phys. Rev. B* **78**, 075120 (2008).
14. V.R. Shaginyan *et al.*, *Phys. Rev. Lett.* **100**, 096406 (2008).
15. J.W. Clark, V.A. Khodel, and M.V. Zverev *Phys. Rev. B* **71**, 012401 (2005).
16. V.R. Shaginyan, M.Ya. Amusia, and K.G. Popov, *Phys. Lett. A* **373**, 2281 (2009).
17. V.R. Shaginyan, M.Ya. Amusia, K.G. Popov, and S.A. Artamonov, *JETP Lett.* **90**, 47 (2009).
18. P. Gegenwart *et al.*, *Science* **315**, 969 (2007).
19. N. Oeschler *et al.*, *Physica B* **403**, 1254 (2008).
20. P. Gegenwart *et al.*, *Physica B* **403**, 1184 (2008).
21. Y. Tokiwa *et al.*, *Phys. Rev. Lett.* **102**, 066401 (2009).
22. L.N. Oliveira, E.K.U. Gross, and W. Kohn, *Phys. Rev. Lett.* **60**, 2430 (1988).
23. V.R. Shaginyan *et al.*, *Europhys. Lett.* **76**, 898 (2006).
24. V.A. Khodel, M.V. Zverev, and V.M. Yakovenko, *Phys. Rev. Lett.* **95**, 236402 (2005).
25. V.R. Shaginyan, *Phys. Lett. A* **249**, 237 (1998).
26. E.M. Lifshitz and L.P. Pitaevskii, *Statistical Physics, Part 2* (Butterworth-Heinemann, Oxford, 1999).
27. M. Pfizner and P. Wölfle, *Phys. Rev. B* **33**, 2003 (1986).
28. D. Wollhardt, P. Wölfle, and P.W. Anderson, *Phys. Rev. B* **35**, 6703 (1987).
29. A. Bianchi *et al.*, *Phys. Rev. Lett.* **91**, 257001 (2003); F. Ronning *et al.*, *Phys. Rev. B* **71**, 104528 (2005).
30. V.R. Shaginyan, K.G. Popov, and V.A. Stephanovich, *Europhys. Lett.* **79**, 47001 (2007).
31. P. Gegenwart, *et al.*, *Phys. Rev. Lett.* **89**, 056402 (2002).
32. D. Takahashi *et al.*, *Phys. Rev. B* **67**, 180407(R) (2003).
33. K. Kadowaki and S.B. Woods, *Solid State Commun.* **58**, 507 (1986).
34. A. Khodel and P. Schuck, *Z. Phys. B: Condens. Matter* **104**, 505 (1997).
35. A.C. Jacko, J.O. Fjærestad, B.J. Powell, *Nature Physics* **5** (2009) 422.
36. V.R. Shaginyan *et al.*, *Phys. Lett. A* **373**, 986 (2009).
37. J. Paglione, *et al.*, *Phys. Rev. Lett.* **91** 246405 (2003).
38. V.R. Shaginyan, M.Ya. Amusia, A.Z. Msezane, K.G. Popov, and V.A. Stephanovich, *Phys. Lett. A* **373**, 986 (2009).
39. M. Neumann, J. Nyéki, and J. Saunders, *Science* **317**, 1356 (2007).
40. Supporting online material for Ref. [39].
41. A. Casey, H. Patel, J. Nyéki, B. P. Cowan, and J. Saunders, *Phys. Rev. Lett.* **90**, 115301 (2003).
42. A.P. Pikul *et al.*, *J. Phys. Condens. Matter* **18**, L535 (2006).

Received 25.09.09

ФЕРМІОННА КОНДЕНСАЦІЯ: НЕЗВИЧАЙНА ІДЕЯ, ЯКА УСПІШНО ПОЯСНЮЄ ПОВЕДІНКУ РІЗНОМАНІТНИХ ФІЗИЧНИХ СИСТЕМ У ПРИРОДІ

В.Р. Шагинян, М.Я. Амусі, К.Г. Попов

Резюме

Сильнокорельовані фермі-системи є найбільш фізично загадковими фундаментальними та добре вивченими експериментально системами, за відсутності, у той же час, їх теоретичного опису. Ідеї, які ґрунтуються на ґратці Кондо та квантових і термічних флуктуаціях, використовуються для пояснення незвичної фізики. Однак, будучи запропонованими для пояснення однієї властивості, ці ідеї виявилися некорисними для пояснення інших властивостей. Такий стан речей вказує на сучасну кризу теорії, для подолання якої нам треба буде відкрити невідомий поки що фундаментальний закон. Теорія ферміон-конденсатного фазового квантового переходу, яка підтримує розширену парадигму квазічастинок і допускає необмежене

зростання ефективної маси як функції температури та напруженості магнітного поля, має змогу вирішити проблему сильнокорельованих систем. Обговорено побудову теорії і показано, що вона дозволяє описати широке коло експериментальних даних в області таких сильнокорельованих систем, як метали з важкими ферміонами та двовимірні фермі-системи. Наш розгляд включає в себе опис вартих уваги експериментів. Проведені обчислення нефермі-рідинної поведінки, термодинамічних і транспортних властивостей та відповідних енергетичних шкал добре узгоджуються з даними. Ці дані виміру теплоємності, на-

магніченості, поздовжнього магнетоопору і магнітної ентропії одержано в унікальних вимірах на металі з важкими ферміонами YbRh_2Si_2 . Продемонстровано, що основні універсальні властивості фазової діаграми температура–густина двовимірного ^3He збігається з відповідними властивостями металів із важкими ферміонами. Запропоновано просту формулу для ефективної маси, яка дозволяє описати універсальні властивості сильнокорельованих систем і пояснити різноманітні експериментальні дані, зібрані у вимірах на ^3He і металах з важкими ферміонами.